Dual-Channel Active Disturbance Injection-Based Islanding Detection Approach for Grid-Forming Converters

Bingtao Zhang, *Student Member, IEEE*, Jinwei He, *Member, IEEE*, and Lucheng Hong, *Senior Member, IEEE*

***Abstract*—To address the issues of large nondetection zones (NDZ) and inaccurate performance evaluation in islanding detection for grid-forming converters, an enhanced islanding detection and evaluation method based on dual-channel active power–voltage magnitude and frequency-disturbance injection is proposed. In proposed approach, islanding faults are determined by simultaneous reaching voltage magnitude and frequency thresholds. With this method, an accurate and rapid islanding detection is obtained in various cases. In addition, compared to traditional approaches, the superior performance of the proposed islanding detection approach has been examined by an accurate small-signal model-based criterion. Different from the NDZ estimation method based on power mismatch, the proposed criterion comprehensively considers the converter control loop and circuitry parameters information, which has higher estimation accuracy. Finally, the feasibility of the proposed approach is verified by experimental evaluation.**

***Index Terms*—Active disturbance injection, grid-forming (GFM) converter, islanding detection, islanding fault, non-detection zone (NDZ).**

I. INTRODUCTION

TO EFFECTIVELY identify the operating status of microgrids, it is important to get fast and accurate islanding fault detection [1] and [2]. Traditional islanding detection methods are mainly classified into two categories, namely, passive detection methods (PDMs) [3], [4], [5], [6], [7] and active detection methods (ADMs) [8], [9], [10], [11], [12]. Compared to PDMs, ADMs detect islanding faults by actively injecting small disturbance signals, resulting in higher detection accuracy and smaller nondetection zone (NDZ). Accordingly, it is intensively studied in recent research.

In the previous research, ADMs are mainly applied to grid-following (GFL) converters [13], [14], [15]. In [13], a two-stage islanding detection method was proposed, where the injected disturbance changes according to instantaneous voltage tracking errors. Then, the islanding fault is judged by the variations of output powers. With this method, the NDZ is reduced at the cost of longer detection time. In [14], the perturbations were injected into the maximum power point tracking algorithm of photovoltaic (PV) converters, where the islanding faults are identified by the degrading of output power rating. Similarly, in this case, the improved islanding detection performance needs more detection time. In addition, by using the recently proposed machine learning algorithms, the load frequency and quality factor were estimated in real time [15]. Then, an active frequency shifting method is applied to achieve an accurate and rapid islanding faults detection. However, the method requires complex computation and data processing, which is a challenge for cost effective converter controllers.

In recent study, the application of grid-forming (GFM) converters to actively support renewable energy grid has received increasing attention [16]. Unlike GFL converters, the output voltage of a GFM converter is influenced by various factors, such as local load, power operation point, and droop coefficient [17]. Accordingly, the aforementioned islanding detection methods for GFL converters may be not applicable to GFM converters.

Some research on islanding detection for GFM converters have been carried out in [18], [19], [20], [21], and [22]. First, a modified droop control with active frequency shift (AFS) method is proposed in [18], where the islanding detection is realized by examining the positive feedback of voltage frequency tracking error. Similarly, a sliding mode frequency shift method based on GFM converters is proposed in [19]. By actively shifting frequency, it achieves islanding fault detection for GFM converters. However, the above methods still have noticeable NDZ. The active harmonic current injection and virtual impedance were applied in [20] to achieve effective islanding detection. However, additional harmonic controller and virtual impedance control make the parameter tuning process more complicated. In summary, existing islanding detection methods for GFM converters still feature challenges, such as complex detection algorithms, long detection times, and large NDZs. In [21], a method based on active negative-sequence current injection is proposed. By detecting the voltage unbalance caused by negative-sequence current injection, islanding faults are identified with a smaller NDZ. However, the injection of negative-sequence current not only degrades the power supply quality but also introduces double-frequency power ripple, adversely

---

Received 14 August 2025; revised 4 November 2025; accepted 29 November 2025. Date of publication 29 December 2025; date of current version 20 March 2026. This work was supported by the Science and Technology Project of State Grid Corporation of China under Grant 5100-202312421A-3-2-ZN. Recommended for publication by Associate Editor S. Golestan. *(Corresponding author: Lucheng Hong.)*

The authors are with the School of Electrical and Information Engineering, Tianjin University, Tianjin 300072, China (e-mail: bingtao.zhang@tju.edu.cn; jinwei.he@tju.edu.cn; hlc3061@seu.edu.cn).

Color versions of one or more figures in this article are available at https://doi.org/10.1109/TPEL.2025.3646222.

Digital Object Identifier 10.1109/TPEL.2025.3646222

affecting system performance. In [22], low-frequency current perturbations are injected into GFM converters with a paralleling active power filter to achieve effective islanding fault detection. The additional equipment and injection of perturbations further increase the cost of this method.

Regarding the estimation of the NDZ, conventional estimation methods evaluate the NDZ by calculating the magnitude of power mismatch in the system [23]. However, this method is only applicable to GFL converters and does not account for the influence of control strategies on power output characteristics. It exhibits significant limitations and proves difficult to apply to GFM converter systems. To address the aforementioned issues, an improved NDZ estimation method is proposed in [24]. In this method, the influence of control strategies and power coupling on power output characteristics is incorporated into the model, thereby enhancing the estimation accuracy of the NDZ. However, the aforementioned method is exclusively focused on traditional islanding detection schemes, and its applicability to other detection methods remains unknown. Furthermore, this approach only considers constant parallel *RLC* loads without accounting for the dynamic characteristics of loads, the NDZ estimation still exhibits conservatism.

In order to further reduce NDZ without increasing the complexity of detection algorithms, an enhanced islanding detection approach based on dual-channel active disturbance injection (Dual-channel ADJ) is proposed for GFM converters. Experimental results have been provided to validate the effectiveness of the proposed detection approach and correctness of the NDZ estimation approach.

In this manuscript, the main contributions include the following.

1) An accurate islanding fault detection method is proposed for single converter. First, dual-channel voltage amplitude and frequency disturbances are injected into the output voltage reference of the system. Then, an accurate islanding fault detection is achieved by synchronously monitoring the amplitude and frequency variations of output voltage, resulting in much smaller NDZ in various conditions.
2) Based on proposed method, false triggering of the detection algorithm is avoided under normal operating conditions, such as grid voltage fluctuations, power steps, and load switching.
3) An accurate NDZ estimation approach is developed without any characteristic approximation. Based on it, the NDZ could be estimated according to the small-signal stability performance of GFM converters in both grid-connected and islanding modes.

II. PROPOSED ISLANDING DETECTION APPROACH

The diagram of a GFM converter with the proposed islanding detection approach is illustrated in Fig. 1. The power circuit as shown in the top part consists of a dc power supply $v_{\rm dc}$, converter bridge, output *LC* filter, local load, and grid $v_{\rm g}$, where $L_{\rm f}$ and $C_{\rm f}$ are the inductance and capacitance of *LC* filter, $z_{\rm g}$ and $z_{\rm L}$ are the grid and load impedance, respectively, and $v_{\rm c}$, $i_{\rm L}$, $i_{\rm o}$, $i_{\rm load}$, and $i_{\rm g}$ are output voltage, converter-side current, output current, load current, and grid current, respectively. The switch *S* is controlled to connect or disconnect the converter from the grid.

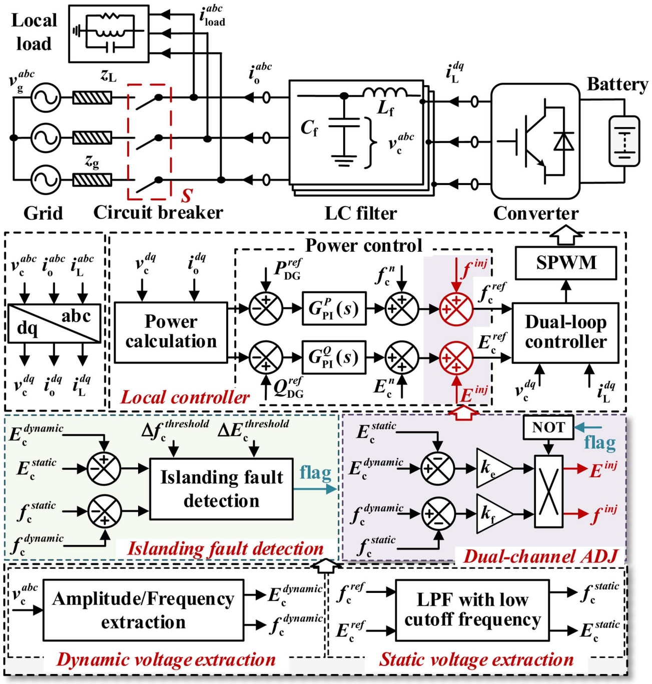

Fig. 1. Diagram of a GFM converter with the proposed islanding detection approach.

The controller is shown in the lower part of Fig. 1, which mainly consists of two parts. The first part is GFM control to emulate the performance of synchronous generators and the second part mainly descripts the disturbance injection and state detection algorithm.

A. Droop Controller With Dual-channel ADJ

First, the output active power $P_{\rm DG}^{\rm lpf}$ and reactive power $Q_{\rm DG}^{\rm lpf}$ of a GFM converter are calculated as

$$\begin{cases} P_{\rm DG}^{lpf} = 1.5\, G_{\rm lpf}(s)\cdot(v_{\rm c}^{d}\cdot i_{\rm o}^{d} + v_{\rm c}^{q}\cdot i_{\rm o}^{q}) \\ Q_{\rm DG}^{lpf} = 1.5\, G_{\rm lpf}(s)\cdot(v_{\rm c}^{q}\cdot i_{\rm o}^{d} - v_{\rm c}^{d}\cdot i_{\rm o}^{q}) \end{cases} \tag{1}$$

where $v_{\rm c}^{dq}$ and i_{o}^{dq} are output voltage and current of the converter, respectively. The subscripts "d and q" represent variables in the synchronous rotating coordinate. The low-pass filter (LPF) $G_{\rm lpf}(s) = \omega_{\rm c}/(s+\omega_{\rm c})$ is applied to filter out ripple components in the instantaneous powers, where $\omega_{\rm c}$ is cutoff frequency.

When output powers are obtained, a modified droop controller with a Dual-channel ADJ is given as

$$\begin{cases} f_{\rm c}^{\rm ref} = f_{\rm c}^{n} + G_{\rm PI}^{P}(s)\cdot(P_{\rm DG}^{\rm ref} - P_{\rm DG}^{\rm lpf}) + f^{\rm inj} \\ E_{\rm c}^{\rm ref} = E_{\rm c}^{n} + G_{\rm PI}^{Q}(s)\cdot(Q_{\rm DG}^{\rm ref} - Q_{\rm DG}^{\rm lpf}) + E^{\rm inj} \end{cases} \tag{2}$$

where the active power droop controller is $G_{\rm PI}^{P}(s) = D^{P} + k_{\rm i}^{P}/s$ and the reactive power droop controller is $G_{\rm PI}^{Q}(s) = D^{Q} + k_{\rm i}^{Q}/s$. $D^{\rm P}$ and $k_{\rm i}^{P}$ are active power droop coefficient and integration coefficient, respectively. D^{Q} and $k_{\rm i}^{Q}$ are reactive power droop coefficient and integration coefficient, respectively. The output voltage amplitude and frequency references are

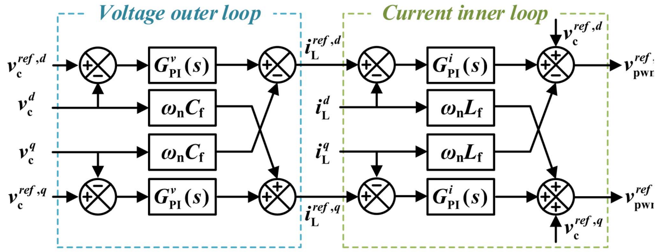

Fig. 2. Detailed control block diagram of a dual-loop controller.

E_c^{ref} and f_c^{ref}. E_c^n and f_c^n are normal voltage magnitude and frequency.

In this modified controller, E^{inj} and f^{inj} are the injected voltage amplitude and frequency disturbances, which are determined according to the differences between the dynamic magnitude E_c^{dynamic} and the static magnitude E_c^{static} of the converter voltage. k_f and k_e are the gains of the disturbance injection terms. A detailed discussion of the functionality of dual-channel disturbance injection is presented in the next section.

When f_c^{ref} is obtained, the phase angle of reference voltage can be given as $\theta_c^{\text{ref}} = 2\pi f_c^{\text{ref}}/s$. Then, the output voltage references $v_c^{\text{ref},d}$ and $v_c^{\text{ref},q}$ are obtained as

$$\begin{cases} v_c^{\text{ref},d} = E_c^{\text{ref}} \\ v_c^{\text{ref},q} = 0. \end{cases} \tag{3}$$

As will be discussed later, the islanding state is detected according to amplification of voltage magnitude and frequency fluctuations in islanding mode. However, these fluctuations can also be created by the droop control in grid-connected mode. In order to avoid misdetection, transient voltage magnitude and frequency variations $\Delta E_c^{\text{droop}}$ and $\Delta f_c^{\text{droop}}$caused by droop control is given

$$\begin{cases} \Delta f_c^{\text{droop}} = D^P(P_{\text{DG}}^{\text{ref}} - P_{\text{DG}}^{\text{lpf}}) \\ \Delta E_c^{\text{droop}} = D^Q(Q_{\text{DG}}^{\text{ref}} - Q_{\text{DG}}^{\text{lpf}}). \end{cases} \tag{4}$$

In a worst grid-connected operation condition, the active and reactive power of the converter are at the minimum value before regulation as $P_{\text{DG}}^{\text{lpf}} = -P_{\text{DG}}^{\text{ref}}$ and $Q_{\text{DG}}^{\text{lpf}} = -Q_{\text{DG}}^{\text{ref}}$, while the active and reactive power references jump to the maximum values as $P_{\text{DG}}^{\text{rex}}$ and $Q_{\text{DG}}^{\text{ref}}$. In this case, the maximum transient voltage magnitude and frequency variations $\Delta E_c^{\max}$ and $\Delta f_c^{\max}$ as:

$$\begin{cases} \Delta f_c^{\max} = 2D^P P_{\text{DG}}^{\text{ref}} \\ \Delta E_c^{\max} = 2D^Q Q_{\text{DG}}^{\text{ref}}. \end{cases} \tag{5}$$

As will be discussed later, the thresholds for islanding detection shall be no less than these values, in order to void misdetection.

B. Voltage and Current Double-Loop Controller

When the output voltage reference $v_c^{\text{ref,dq}}$ is obtained, a voltage and current dual-loop controller is adopted to achieve accurate tracking of converter voltage. The detailed control block diagram of a dual-loop controller is shown in Fig. 2.

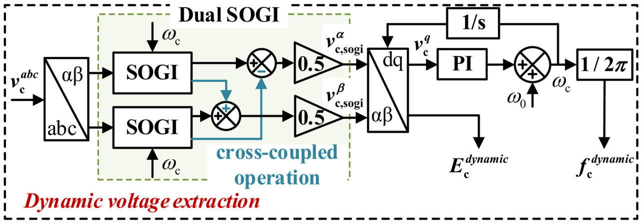

Fig. 3. Diagram of dynamic voltage extraction based on DSOGI.

First, the outer voltage tracking loop adopts a proportional–integral (PI) controller as

$$i_L^{\text{ref,dq}} = G_{\text{PI}}^v(s) \cdot (v_c^{\text{ref,dq}} - v_c^{\text{dq}}) = \left(k_p^v + \frac{k_i^v}{s}\right) \cdot (v_c^{\text{ref,dq}} - v_c^{\text{dq}}) \tag{6}$$

where $G_{\text{PI}}^v(s)$ is the transfer function of PI controller, k_p^v and k_i^v are correspondingly proportional and integral coefficient, and $i_L^{\text{ref,dq}}$ is the output current reference of current inner loop.

Then, a PI controller is adopted in the current tracking loop. In order to enhance the voltage control performance, the output voltage reference $v_c^{\text{ref,dq}}$ from power controller is added as a feedforward term

$$\begin{aligned} v_{\text{pwm}}^{\text{ref,dq}} &= G_{\text{PI}}^i(s) \cdot (i_L^{\text{ref,dq}} - i_L^{\text{dq}}) + v_c^{\text{ref,dq}} \\ &= \left(k_p^i + \frac{k_i^i}{s}\right) \cdot (i_L^{\text{ref,dq}} - i_L^{\text{dq}}) + v_c^{\text{ref,dq}} \end{aligned} \tag{7}$$

where $G_{\text{PI}}^i(s)$ is the transfer function of current inter loop controller, k_p^i and k_i^i are corresponding proportional coefficient and integral coefficient, respectively. The output is the reference voltage $v_{\text{pwm}}^{\text{ref,dq}}$ for modulation.

C. Proposed Islanding Detection Approach

With the Dual-channel ADJ as shown above, the detailed islanding detection process can be designed accordingly.

a) Dual-channel ADJ: First, based on the output voltage amplitude and frequency disturbances obtained at the previous moment, they are injected into the adopted power control loop in (2) to obtain the output voltage amplitude and frequency references $E_c^{\text{ref}}$and f_c^{ref}.

b) Dynamic voltage extraction: Based on local control, the obtained $E_c^{\text{ref}}$and f_c^{ref} are applied to the GFM converter system to obtain the instantaneous output voltage v_c^{abc} at the current moment. Then, a dual second-order generalized integrator (DSOGI) [25], [26] is applied to extract dynamic amplitude E_c^{dynamic} and frequency f_c^{dynamic} of output voltage v_c, as shown in Fig. 3.

c) Static voltage extraction: Then, a LPF with low cutoff frequency is applied to extract static output voltage amplitude E_c^{static} and frequency f_c^{static} from the obtained reference E_c^{ref} and f_c^{ref}, as follows:

$$\begin{cases} E_c^{\text{static}} = G_{\text{lpf}}^{\text{low}}(s) \cdot E_c^{\text{ref}} \\ f_c^{\text{static}} = G_{\text{lpf}}^{\text{low}}(s) \cdot f_c^{\text{ref}} \end{cases} \tag{8}$$

where $G_{\text{lpf}}^{\text{low}}(s)$ is the transfer function of the low cutoff frequency LPF.

d) Islanding fault detection: When an islanding fault occurs, the GFM system can still operate to provide voltage and frequency support. However, it normally moves to a new steady-state operating point [16]. To ensure an accurate islanding detection, the absolute deviations between dynamic values and static values of voltage amplitude and frequency are captured as $\Delta E_{\mathrm{c}}^{\mathrm{error}}$ and $\Delta f_{\mathrm{c}}^{\mathrm{error}}$, respectively

$$\begin{cases}\Delta E_{\mathrm{c}}^{\mathrm{error}} = abs(E_{\mathrm{c}}^{\mathrm{dynamic}} - E_{\mathrm{c}}^{\mathrm{static}})\\ \Delta f_{\mathrm{c}}^{\mathrm{error}} = abs(f_{\mathrm{c}}^{\mathrm{dynamic}} - f_{\mathrm{c}}^{\mathrm{static}}).\end{cases} \tag{9}$$

Then, when the $\Delta E_{\mathrm{c}}^{\mathrm{error}}$ and $\Delta f_{\mathrm{c}}^{\mathrm{error}}$ both reach their corresponding thresholds, the islanding operation of the GFM converter is confirmed as

$$\mathrm{flag} = (\Delta E_{\mathrm{c}}^{\mathrm{error}} \geq \Delta E_{\mathrm{c}}^{\mathrm{threshold}})\&\&(\Delta f_{\mathrm{c}}^{\mathrm{error}} \geq \Delta f_{\mathrm{c}}^{\mathrm{threshold}}) \tag{10}$$

where the symbol "&" is "and" operator, flag is an islanding flag signal. When the islanding fault is identified, the islanding flag signal flag is set to 1. Then, the small disturbances E^{inj} and f^{inj} is disabled to avoid excessive oscillation.

It should be noted that when selecting the fluctuation thresholds $\Delta E_{\mathrm{c}}^{\mathrm{threshold}}$ and $\Delta f_{\mathrm{c}}^{\mathrm{threshold}}$, the thresholds of voltage amplitudes and frequency deviation for islanding detection shall be carefully designed to avoid the false triggering of islanding detection. According to (5), in theory, the thresholds of voltage magnitude and frequency for islanding detection should be higher than maximum fluctuation caused by droop control as shown below:

$$\begin{cases}\Delta f_{\mathrm{c}}^{\mathrm{threshold}} > \Delta f_{\mathrm{c}}^{\mathrm{max}}\\ \Delta E_{\mathrm{c}}^{\mathrm{threshold}} > \Delta f_{\mathrm{c}}^{\mathrm{max}}.\end{cases} \tag{11}$$

In practice, considering other types of disturbances, such as voltage tracking error and noises always exist, the thresholds $\Delta E_{\mathrm{c}}^{\mathrm{threshold}}$ and $\Delta f_{\mathrm{c}}^{\mathrm{threshold}}$ should be sufficiently higher than the maximum transient fluctuations caused by droop control as $\Delta E_{\mathrm{c}}^{\mathrm{max}}$ and $\Delta f_{\mathrm{c}}^{\mathrm{max}}$.

e) Disturbance calculation and update: Based on $E_{\mathrm{c}}^{\mathrm{dynamic}}$, $f_{\mathrm{c}}^{\mathrm{dynamic}}$, $E_{\mathrm{c}}^{\mathrm{static}}$, and $f_{\mathrm{c}}^{\mathrm{static}}$ at the current moment, the injected voltage amplitude disturbance E^{inj} and frequency disturbance f^{inj} are calculated for the next moment's disturbance injection. The calculation formulas are as follows:

$$\begin{cases}E^{\mathrm{inj}} = k_{\mathrm{e}}(E_{\mathrm{c}}^{\mathrm{dynamic}} - E_{\mathrm{c}}^{\mathrm{static}})\\ f^{\mathrm{inj}} = k_{\mathrm{f}}(f_{\mathrm{c}}^{\mathrm{dynamic}} - f_{\mathrm{c}}^{\mathrm{static}}).\end{cases} \tag{12}$$

Finally, to get a better understanding of the proposed islanding detection approach, the detailed flow chart of the proposed detection process is shown in Fig. 4.

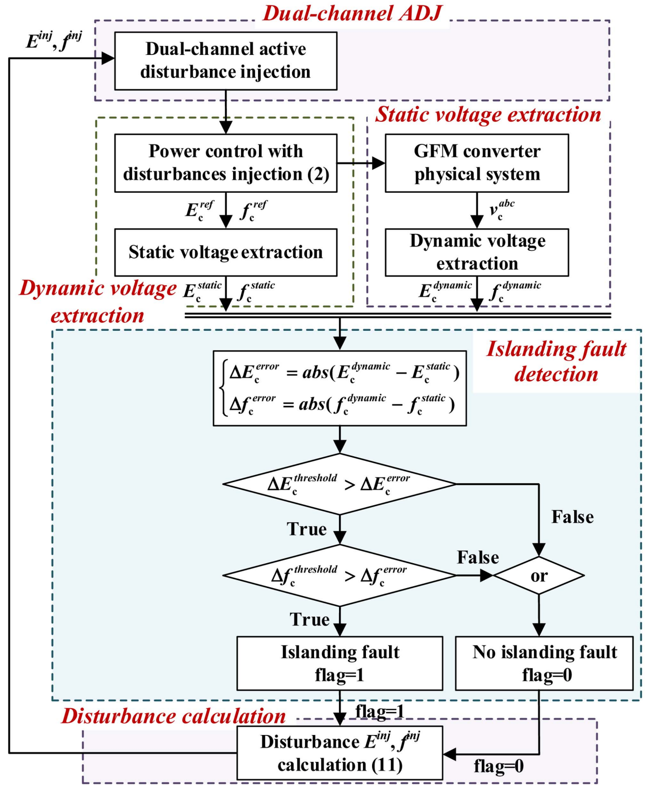

Fig. 4. Flowchart of the proposed islanding detection approach.

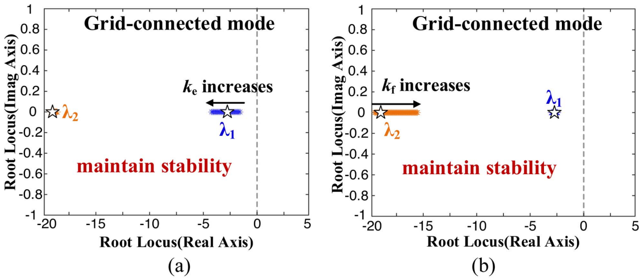

Fig. 5. Root loci under grid-connected mode when the disturbance coefficient varies. (a) $1e - 4 < k_e < 1.5$. (b) $1e - 2 < k_f < 0.5$ rad/(V.s).

III. SYSTEM CHARACTERISTICS ANALYSIS

A. Small-Signal Model and Detection Accuracy Analysis

To evaluate the effectiveness of the proposed islanding detection algorithm, small-signal models of the system in grid-connected and islanding modes are established in this section. In this analysis, the voltage tracking dynamics of the GFM converter is ignored and it is modeled as an ideal controlled voltage source.

Considering small disturbances in the system as $\Delta\theta_{\mathrm{c}}$ and ΔE_{c}, according to the modified droop controller and the power flow relationships between the GFM converter and grid equivalent voltage source, the small-signal model of the system in grid-connected mode is expressed as

$$[M_1 M_2 M_3 - I] \cdot x = 0 \tag{13}$$

where the state variables $x = [\Delta\theta_{\mathrm{c}}, \Delta E_{\mathrm{c}}]^T$, the symbol "$\Delta$" represents small disturbances. The detailed expressions of matrices M_1, M_2 and M_3 can be seen in Appendix.

Similarly, the small-signal model of the system in islanding mode is given as

$$[N_1 N_2 N_3 - I] \cdot x = 0 \tag{14}$$

where the detailed expressions of matrices N_1, N_2, and N_3 can be found in Appendix.

When small-signal models of the system are obtained, the system root loci with varying control parameters can be obtained in Figs. 5 and 6. To make the discussion more straightforward, only the dominated pole pair is presented, where, the white star

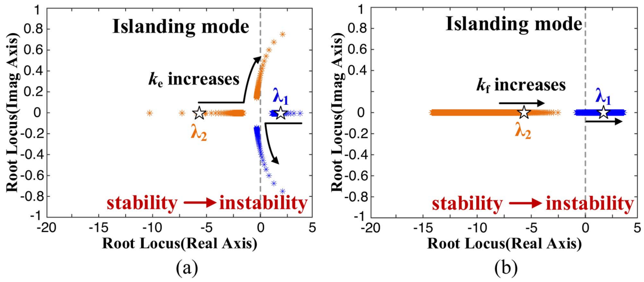

(a) (b)

Fig. 6. Root loci under islanding mode when the disturbance coefficient varies. (a) $1e-4 < k_e < 1.5$. (b) $1e-2 < k_f < 0.5$ rad/(V.s).

represents the transient operating point of the system under the set parameters.

First, in grid-connected mode, the dominated root loci of the system are presented in Fig. 5. As seen in Fig. 5(a), there are two dominated root loci λ_1 and λ_2, which are located at the left half plane. When the disturbance coefficient k_e changes from 1e-4 to 1.5, λ_1 moves away from the imaginary axis while λ_2 is roughly unchanged. Similarly, when the frequency disturbance coefficient k_f increases from 1e-2 rad/(V.s) to 0.5 rad/(V.s), λ_2 moves to the right while λ_1 is almost unchanged, as shown in Fig. 5(b). This indicates that in the given parameter ranges, the grid-connected operation of the system is always stable.

In addition, the performances of the system in islanding mode are presented in Fig. 6. In this case, λ_1 is located on the right side of the imaginary axis when k_e is small. In addition, when k_e becomes large, λ_2 also becomes an unstable pole. Similarly, when k_f gradually increases from 1e-2 rad/(V.s) to 0.5 rad/(V.s), in most of the cases, λ_1 is located on right side of the imaginary axis. This indicates that the system can be easily unstable with the given parameter ranges.

When the system is always stable in grid-connected mode but unstable in islanding mode, the amplifications of voltage magnitude and frequency oscillations in the islanding mode can be captured as an indicator to determine the state transitions. This can also be described as

$$\begin{cases} \lambda < 0, & \text{stable in grid-connected mode} \\ \lambda > 0, & \text{unstable in islanding mode} \end{cases} \tag{15}$$

where λ is the maximum value of system dominated roots' real parts as

$$\lambda = \max\left(\mathrm{Real}(\lambda_1), \mathrm{Real}(\lambda_2)\right). \tag{16}$$

For all types of GFM converters, the islanding detection is correct when (15) is satisfied. Otherwise, the system has misdetection zones or NDZs. Note that the NDZ estimation approach as shown above is determined based on vigorous model with the impacts of control loops, circuitry configuration, and local loads information included. Accordingly, it is more accurate compared to NDZ calculation method based on power deviations [23], [24]. However, due to the space limitation, a detailed comparison between these approaches is not presented here.

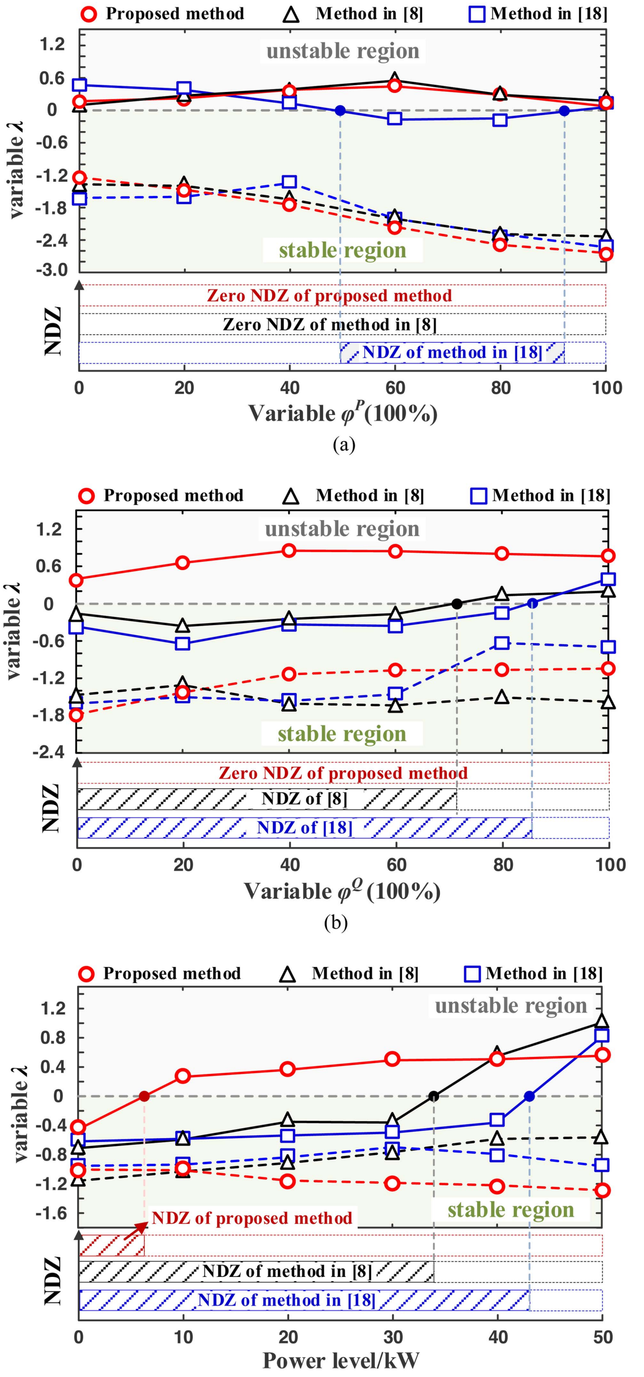

(a)

(b)

(c)

Fig. 7. Variation of the λ under different conditions. (Dashed line: grid-connected mode, solid line: islanding mode; shaded block: NDZ.). (a) NDZ with varying φ^P from 0% to 100% ($\varphi^Q = 100\%$). (b) NDZ with varying φ^Q from 0% to 100% ($\varphi^P = 100\%$). (c) NDZ with varying system power level from 0 kW to 50 kW under source-load balanced condition ($\varphi^P = 100\%$ and $\varphi^Q = 100\%$).

B. *Discussion and Comparisons*

Based on the definitions of an effective criterion in (14) and (15), the NDZs of the system using traditional AVS in [8], AFS in [18] and the proposed method are compared, as shown in Fig. 7. In this figure, active and reactive load factor φ^P and φ^Q

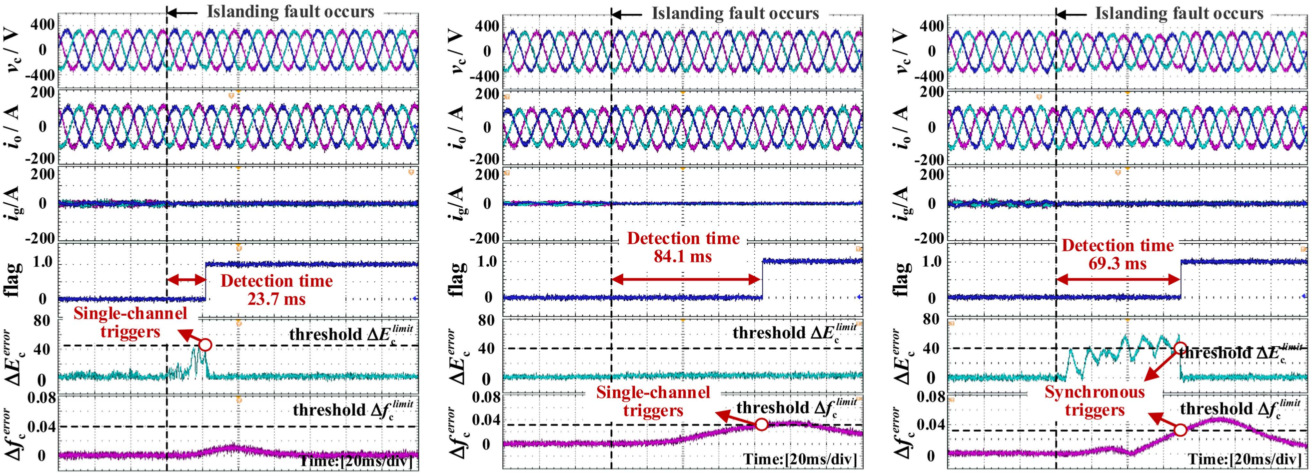

(a) (b) (c)

Fig. 8. System performances in source-load balance condition ($\varphi^P = 100\%$ and $\varphi^Q = 100\%$; $P_{\mathrm{DG}} = 50$ kW, and $Q_{\mathrm{DG}} = 50$ kVar in grid-connected mode). (a) AVS method in [8]. (b) AFS method in [18]. (c) Proposed method.

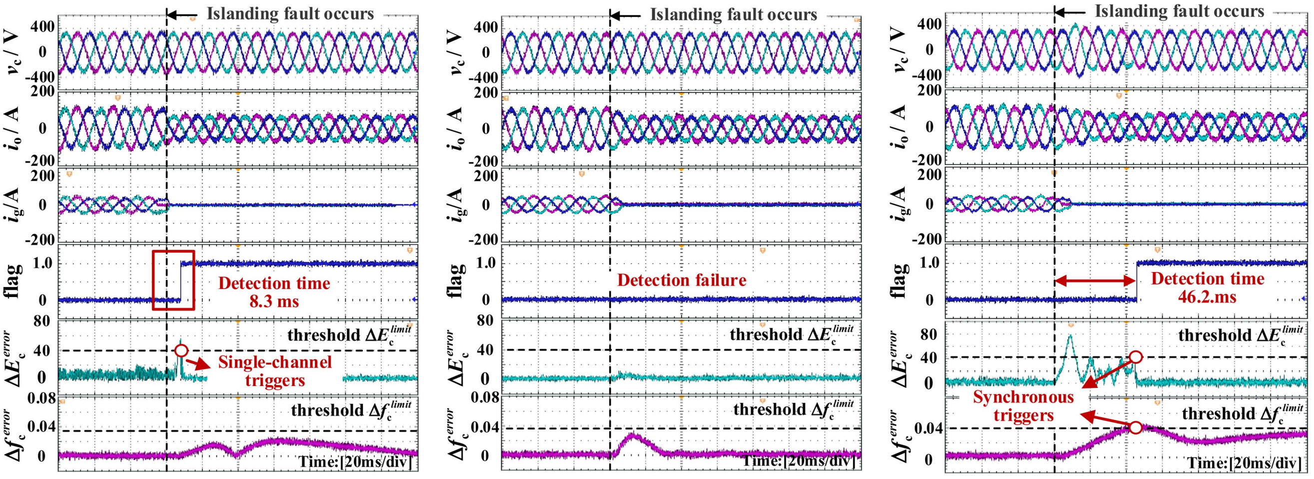

(a) (b) (c)

Fig. 9. System performances when φ^P is 60% and $\varphi^Q = 100\%$ ($P_{\mathrm{DG}} = 50$ kW and $Q_{\mathrm{DG}} = 50$ kVar in grid-connected mode). (a) AVS method in [8]. (b) AFS method in [18]. (c) Proposed method.

are defined by the percentage of local load power to converter static output power in grid-connected mode as $\varphi^P = (P_{\mathrm{L}}/\mathrm{P}_{\mathrm{DG}}^{\mathrm{ref}}) * 100\%$ and $\varphi^Q = (Q_{\mathrm{L}}/\mathrm{Q}_{\mathrm{DG}}^{\mathrm{ref}}) * 100\%$. The solid line represents the system performance in islanding mode and the dashed line represents the system performance in grid-connected mode. As shown in the bottom of each figure, the shaded block stands for the NDZ of each approach.

First, when the active load factor φ^P changes from 0% to 100% and φ^Q is fixed to 100%, the variables λ with different detection methods are presented in Fig. 7(a), where the solid line is always below zero and the dashed line is always above zero. This indicates both systems can effectively detect islanding faults with zero NDZ performance. However, with the traditional AFS method in [18], there is nontrivial NDZ, ranging from around 50% to 90% φ^P. Similarly, when the φ^Q changes from 0% to 100% and φ^P is 100%, the variables λ with both traditional methods and the proposed method are shown in Fig. 7(b). As shown, as φ^Q gradually increases, the systems with the traditional AVS and AFS methods have relatively large NDZs. Once again, there is zero NDZ of the system with the proposed approach.

Furthermore, when the system has different output power levels and it always works in source-load balance condition ($\varphi^P = 100\%$ and $\varphi^Q = 100\%$), the variables λ with different methods are presented in Fig. 7(c). It is seen that even in the adverse condition, NDZ using the proposed approach is still much smaller than that of traditional detection methods in [8] and [18].

IV. PERFORMANCE EVALUATION

The effectiveness of the proposed islanding detection approach is further verified on the established three-phase two-level power converter experimental platform, as shown in Fig. 14.

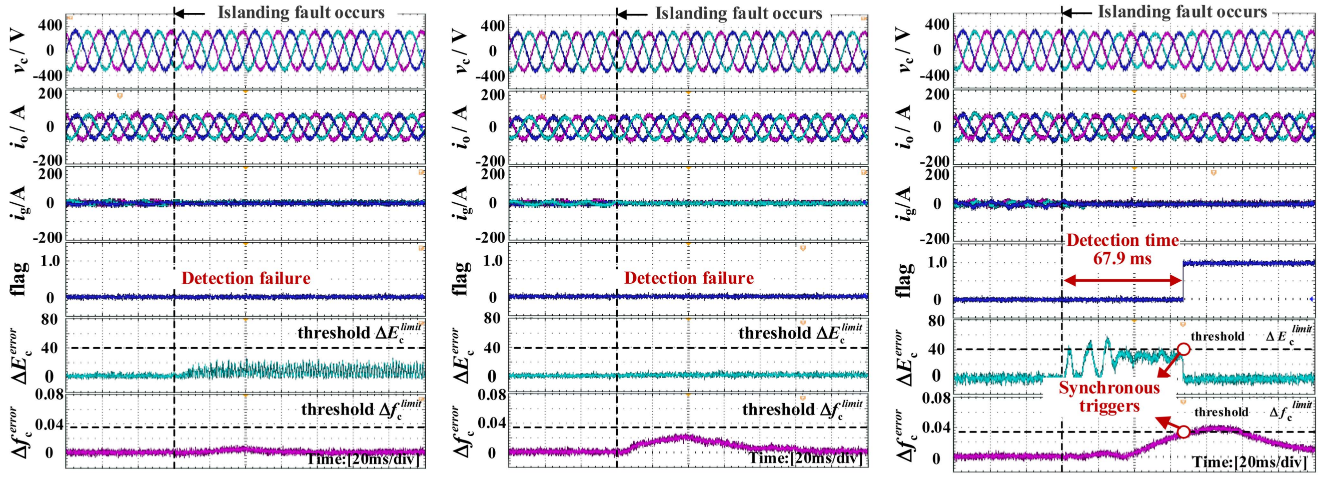

(a) (b) (c)

Fig. 10. System performances in source-load balance condition ($\varphi^P = 100\%$ and $\varphi^Q = 100\%$; $P_{\text{DG}} = 30$ kW and $Q_{\text{DG}} = 50$ kVar in grid-connected mode). (a) AVS method in [8]. (b) AFS method in [18]. (c) Proposed method.

The parameters of the system are illustrated in Table II. Note that to avoid the unstable operation of the GFM converter under islanding mode, the active disturbance injection is disable when the islanding mode is confirmed by the controller.

A. *Evaluation of Islanding Detection Characteristic*

By using traditional AVS, AFS and the proposed approaches, experimental waveforms of the converter are presented and compared in Figs. 8–10. In the three groups of tests, the load current, grid current, islanding flag signal, output voltage amplitude, and frequency fluctuations are given from top to bottom.

First, the power reference of the converter at grid-connected mode is set to 50 kW and 50 kVar. The active load factor φ^P and φ^Q are both at 100%. The performances of the system with different detection methods are shown in Fig. 8. It can be seen that with traditional AVS method in [8], AFS method in [18], and the proposed method, the detection times are 23.7, 84.1, and 69.30 ms, respectively. They are all far less than 2 s of the corresponding IEEE standard [27].

In addition, when the active load factor φ^P reduces to 60% and φ^Q still at 100%, system performances using three detection methods are shown in Fig. 9. It can be seen that with the AVS method in [8] and the proposed method, the detection times are 8.3 and 46.2 ms, respectively. This is because the dual-channel synchronous judgment takes longer time in the proposed approach. On the other hand, the islanding faults cannot be detected out with the AFS method in [18]. This is consistent with Fig. 7.

When the power reference of the converter at grid-connected mode is set to 30 kW and the φ^P and φ^Q are still at 100%, in this case, similar experiments are conducted in Fig. 10. it is seen that the islanding faults of the system cannot be detected with traditional methods in [8] and [18], while the proposed method can still quickly detect islanding faults within 67.9 ms.

From the above discussion, it is seen that the NDZ of proposed method is smaller comparing the traditional islanding detection methods, which has a good agreement with theoretical analysis in Section III.

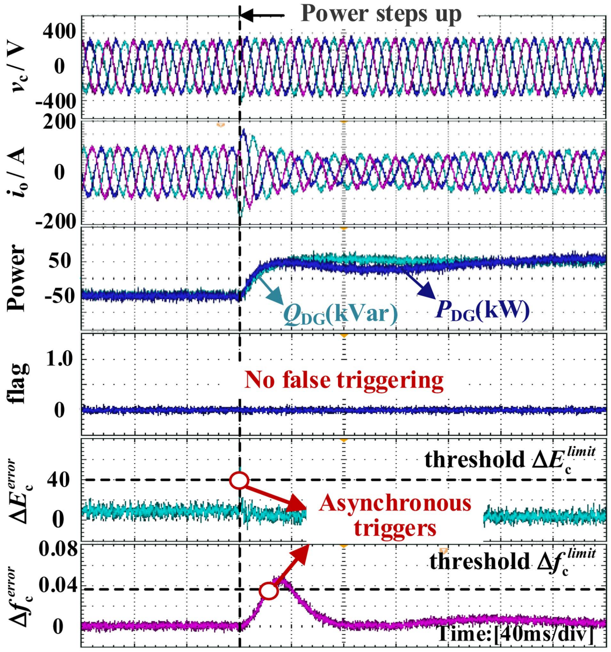

Fig. 11. Anti-false triggering performance of the system during power references jump from −50 to 50 in grid-connected condition.

B. *Evaluation of Anti-False Triggering Characteristic*

The anti-false triggering performance is another factor that needs to be validated. Figs. 11–13 show the experimental anti-false triggering performance of a grid-connected operation system using the proposed approach. It should be noted that, the droop coefficients are designed in this article to verify the harsh working conditions according to (5), which is fairly close to the boundary. In actual adjustment process, due to the influence of the noise, parameter randomness and system dynamics, the

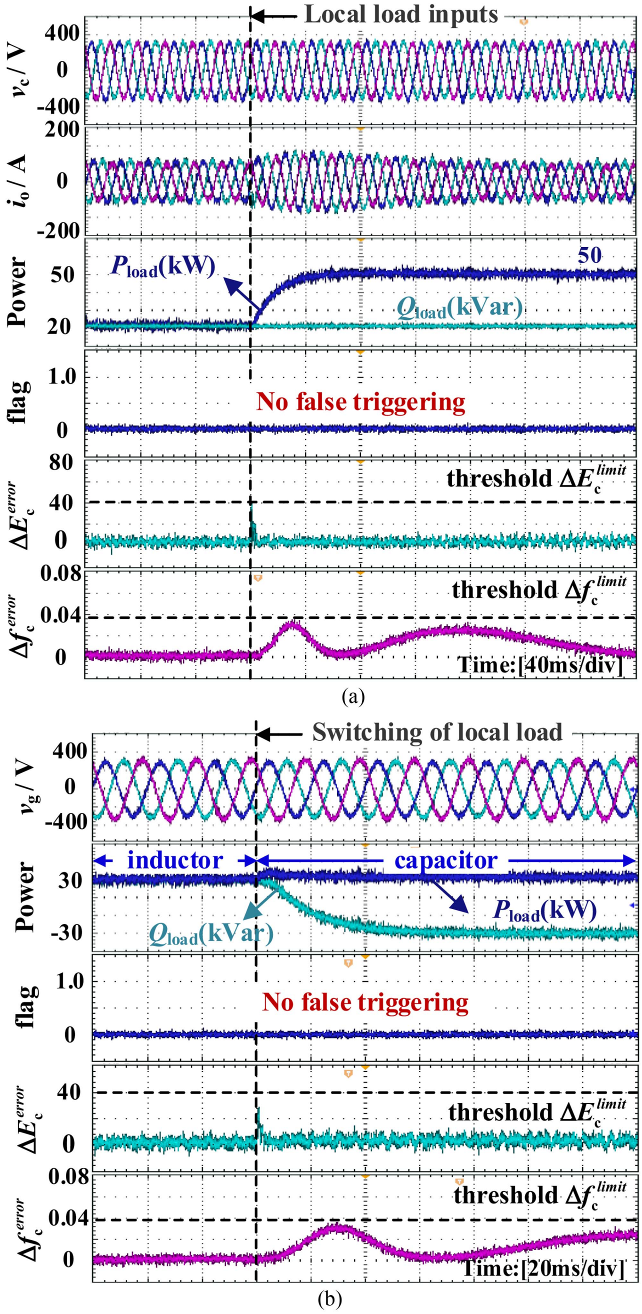

(a)

(b)

Fig. 12. Anti-false triggering performance of the system during local load varying in grid-connected condition. (a) System performance during local load inputs. (b) System performance during local load performance switching.

fluctuations of output voltage amplitude and frequency will slightly exceed the thresholds. However, in this article, due to the multiple judgments of voltage amplitude and frequency fluctuations, the system will not be falsely triggered under normal operating conditions.

1) Operating condition with output power variation: First, when power references of the system step up from −50 to 50 kW/kVar, the transient amplitude and frequency fluctuations of output voltage are shown in Fig. 11. It can be seen that they do not exceed the threshold at the same time, and the system has no risk of false triggering.

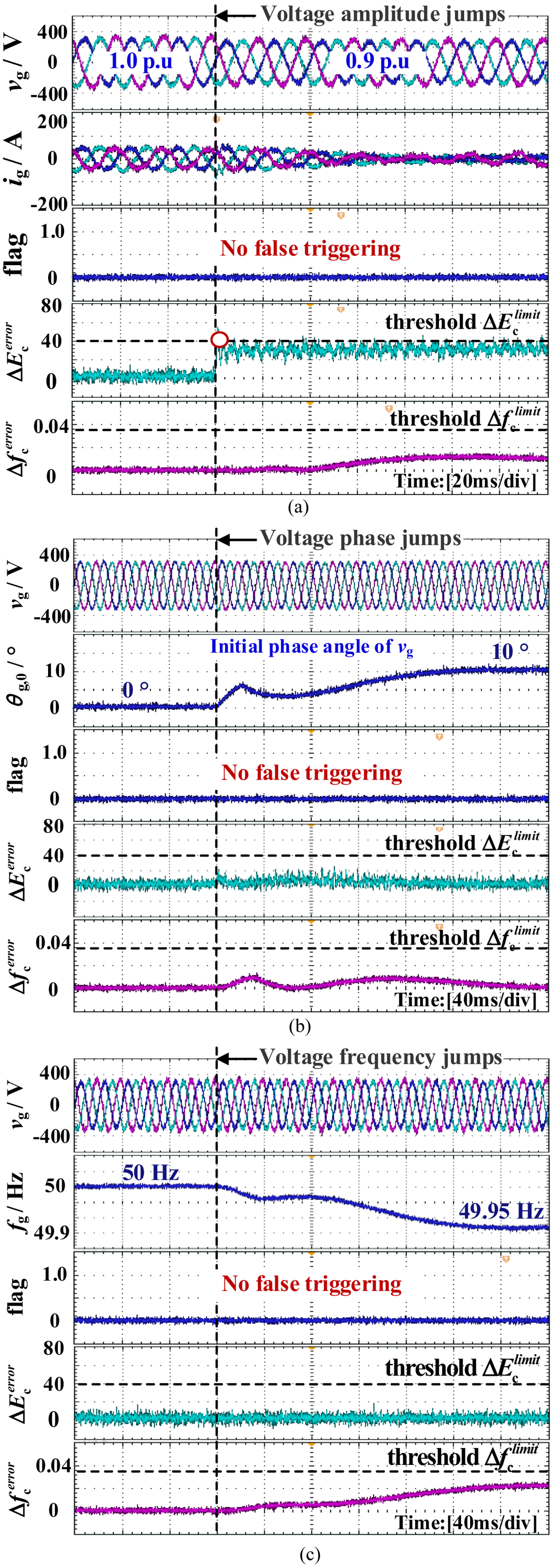

(a)

(b)

(c)

Fig. 13. Anti-false triggering performance of the system during grid voltage varying in grid-connected condition. (a) System performance during grid voltage amplitude jumps. (b) System performance during grid voltage initial phase angle jumps. (c) System performance during gird voltage frequency jumps.

TABLE I
COMPARISON RESULTS OF COMMON ACTIVE ISLANDING DETECTION METHODS

Methods	**Detection time**	**NDZ**	**Possibility of false triggering**	**Impact on power quality**
AVS in [8]	short	large	high	medium
AFS in [18]	long	medium	high	small
Method in [19]	medium	medium	high	small
SACS in [20]	medium	small	low	big
Method in [21]	slow	small	medium	medium
Method in [22]	slow	small	medium	medium
proposed method	medium	small	low	medium

2) Operating conditions with local load variation: Similarly, when the local load power changes (P_{load} from 20 to 50 kW), the system will not falsely trigger the proposed islanding detection algorithm, as shown in Fig. 12(a). Furthermore, when the local load switches from inductive to capacitive, the system output waveforms are shown in Fig. 12(b). At this time, only the output voltage magnitude exceeds the threshold, while the change in output voltage frequency does not reach the threshold. Therefore, the proposed islanding detection algorithm is still not falsely triggered when the load characteristics change.

3) Operating conditions with grid voltage variation: On the other hand, the impact of grid voltage variations on the detection reliability of the proposed islanding detection algorithm is also considered, as shown in Fig. 13. It can be observed that changes in the amplitude, phase, and frequency of the grid voltage do not cause false triggering of the proposed islanding detection algorithm. The results in Figs. 11–13 are consistent with the above analysis.

In summary, under the aforementioned operating conditions, the proposed islanding detection algorithm is not falsely triggered, demonstrating high detection accuracy.

In addition, the control characteristics of several common active islanding detection methods are summarized in Table I. It can be found that comprehensively considering the detection time, NDZ, anti-false triggering characteristic and impact on power quality, the proposed approach is superior to that of these traditional methods.

V. CONCLUSION

In this article, an enhanced islanding detection and evaluation approach based on Dual-channel ADJ for a GFM converter is proposed. The contribution and merit of this article are summarized: 1) With the Dual-channel ADJ and amplitude-frequency synchronous detection, the proposed method can achieve more accurate islanding detection with a smaller NDZ. 2) An accurate NDZ estimation approach is developed according to the small-signal stability performance of the GFM converter in both grid-connected and islanding modes. The experiment results have shown a good agreement with the proposed islanding detection and the NDZ estimation approach.

It should be noted that the islanding detection evaluation method proposed in this article is only a preliminary exploration. In future research, further studies will be conducted on high-performance islanding detection technologies for complex systems.

APPENDIX

A. Small-Signal Model in Grid-Connected Model

When the GFM converter operates in grid-connected mode, and assuming the output voltage of the converter, grid voltage, load impedance, and grid impedance are expressed as $v_{\mathrm{c}} = E_{\mathrm{c}}e^{\mathrm{j}\theta_{\mathrm{c}}}$, $v_{\mathrm{g}} = E_{\mathrm{g}}e^{\mathrm{j}\theta_{\mathrm{g}}}$, $z_{\mathrm{L}} = Z_{\mathrm{L}}e^{\mathrm{j}\varphi_{\mathrm{L}}}$, and $z_{\mathrm{g}} = Z_{\mathrm{g}}e^{\mathrm{j}\varphi_{\mathrm{g}}}$, respectively, the apparent power $\vec{S}_{\mathrm{DG}} = P_{\mathrm{DG}} + jQ_{\mathrm{DG}}$ can be obtained as [16]

$$\vec{S}_{\mathrm{DG}} = v_{\mathrm{c}} \cdot i_{\mathrm{o}}^{*} = \frac{(E_{\mathrm{c}})^2}{Z_{\mathrm{L}}}e^{j\varphi_{\mathrm{L}}} + \frac{(E_{\mathrm{c}})^2}{Z_{\mathrm{g}}}e^{j(\varphi_{\mathrm{g}}-\theta_{\mathrm{g}})} - \frac{E_{\mathrm{c}}E_{\mathrm{g}}}{Z_{\mathrm{g}}}e^{j\theta_{\mathrm{c}}} \tag{A1}$$

where the symbol “$*$” indicates the conjugated values of variables. Z and φ are the amplitude and impedance angle of the corresponding impedance. E and θ are the amplitude and phase angle of corresponding voltages.

According to (A1), the power variations ΔP_{DG} and ΔQ_{DG} of the converter can be obtained as

$$\begin{aligned} \Delta P_{\mathrm{DG}} &= \mathrm{Re}(\Delta\vec{S}_{\mathrm{DG}}) \\ &= \mathrm{Re}(\partial\vec{S}_{\mathrm{DG}}/\partial\theta_{\mathrm{c}}) \cdot \Delta\theta_{\mathrm{c}} + \mathrm{Re}(\partial\vec{S}_{\mathrm{DG}}/\partial E_{\mathrm{c}}) \cdot \Delta E_{\mathrm{c}} \\ \Delta Q_{\mathrm{DG}} &= \mathrm{Im}(\Delta\vec{S}) \\ &= \mathrm{Im}(\partial\vec{S}_{\mathrm{DG}}/\partial\theta_{\mathrm{c}}) \cdot \Delta\theta_{\mathrm{c}} + \mathrm{Im}(\partial\vec{S}_{\mathrm{DG}}/\partial E_{\mathrm{c}}) \cdot \Delta E_{\mathrm{c}} \end{aligned} \tag{A2}$$

where Re and Im represent the real and imaginary parts of complex numbers.

When there is a small disturbance at the equilibrium point, small-signal equation of the GFM converter droop controller (2) is shown as

$$\begin{cases} \Delta\theta_{\mathrm{c}} = -\frac{G_{\mathrm{PI}}^{P}(s)}{s}\Delta P_{\mathrm{DG}}^{\mathrm{lpf}} - \frac{k_{\mathrm{f}}G_{\mathrm{PI}}^{Q}(s)}{(1-k_{\mathrm{e}})s}\Delta Q_{\mathrm{DG}}^{\mathrm{lpf}} \\ \Delta E_{\mathrm{c}} = -\frac{G_{\mathrm{PI}}^{Q}(s)}{1-k_{\mathrm{e}}}\Delta Q_{\mathrm{DG}}^{\mathrm{lpf}} \end{cases} \tag{A3}$$

where $\Delta P_{\mathrm{DG}}^{\mathrm{lpf}} = G_{\mathrm{lpf}}(s)\Delta P_{\mathrm{lpf}}$ and $\Delta Q_{\mathrm{DG}}^{\mathrm{lpf}} = G_{\mathrm{lpf}}(s)\Delta Q_{\mathrm{lpf}}$ are the small-signal output power variations of the converter after low-pass filtering, respectively.

According to [29] and [30] and by combining (A1)–(A3), the small-signal model of the GFM system in grid-connected mode is obtained as

$$(M_1M_2M_3 - I) \cdot \begin{bmatrix} \Delta\theta_{\mathrm{c}} \\ \Delta E_{\mathrm{c}} \end{bmatrix} = 0 \tag{A4}$$

where M_1, M_2, and M_3 are the system matrixes, and I is an identity matrix. The detailed elements of matrix are as follows:

$$M_1 = \begin{bmatrix} -\frac{G_{\mathrm{PI}}^{P}(s)G_{\mathrm{lpf}}(s)}{s} & -\frac{G_{\mathrm{PI}}^{Q}(s)\cdot G_{\mathrm{lpf}}(s)k_{\mathrm{f}}}{s(1-k_{\mathrm{e}})} \\ 0 & -\frac{G_{\mathrm{PI}}^{Q}(s)\cdot G_{\mathrm{lpf}}(s)}{1-k_{\mathrm{e}}} \end{bmatrix},$$

$$M_3 = \begin{bmatrix} -E_{\mathrm{c}}\sin\theta_{\mathrm{c}} & \cos\theta_{\mathrm{c}} \\ E_{\mathrm{c}}\cos\theta_{\mathrm{c}} & \sin\theta_{\mathrm{c}} \\ \frac{\partial i_{\mathrm{o}}^{d}}{\partial\theta_{\mathrm{c}}} & \frac{\partial i_{\mathrm{o}}^{d}}{\partial E_{\mathrm{c}}} \\ \frac{\partial i_{\mathrm{o}}^{q}}{\partial\theta_{\mathrm{c}}} & \frac{\partial i_{\mathrm{o}}^{q}}{\partial E_{\mathrm{c}}} \end{bmatrix}$$

$$M_2 = \begin{bmatrix} 1.5i_{\mathrm{o}}^{d} & 1.5i_{\mathrm{o}}^{q} & 1.5v_{\mathrm{c}}^{d} & 1.5v_{\mathrm{c}}^{q} \\ -1.5i_{\mathrm{o}}^{q} & 1.5i_{\mathrm{o}}^{d} & 1.5v_{\mathrm{c}}^{q} & -1.5v_{\mathrm{c}}^{d} \end{bmatrix}, I = \begin{bmatrix} 1 & 0 \\ 0 & 1 \end{bmatrix}$$

$$\frac{\partial i_{\mathrm{o}}^{d}}{\partial \theta_{\mathrm{c}}} = E_{\mathrm{c}} \left(\frac{\cos\theta_{\mathrm{c}} \sin\varphi_{\mathrm{g}} - \sin\theta_{\mathrm{c}} \cos\varphi_{\mathrm{g}}}{Z_{\mathrm{g}}} + \frac{\cos\theta_{\mathrm{c}} \sin\varphi_{\mathrm{L}} - \sin\theta_{\mathrm{c}} \cos\varphi_{\mathrm{L}}}{Z_{\mathrm{L}}} \right);$$

$$\frac{\partial i_{\mathrm{o}}^{d}}{\partial E_{\mathrm{c}}} = \frac{\cos\theta_{\mathrm{c}} \cos\varphi_{\mathrm{g}} + \sin\theta_{\mathrm{c}} \sin\varphi_{\mathrm{g}}}{Z_{\mathrm{g}}} + \frac{\cos\theta_{\mathrm{c}} \cos\varphi_{\mathrm{L}} + \sin\theta_{\mathrm{c}} \sin\varphi_{\mathrm{L}}}{Z_{\mathrm{L}}};$$

$$\frac{\partial i_{\mathrm{o}}^{q}}{\partial \theta_{\mathrm{c}}} = E_{\mathrm{c}} \left(\frac{\cos\theta_{\mathrm{c}} \cos\varphi_{\mathrm{g}} + E_{\mathrm{c,n}} \sin\theta_{\mathrm{c}} \sin\varphi_{\mathrm{g}}}{Z_{\mathrm{g}}} + \frac{\sin\theta_{\mathrm{c}} \sin\varphi_{\mathrm{L}} + \cos\theta_{\mathrm{c}} \cos\varphi_{\mathrm{L}}}{Z_{\mathrm{L}}} \right);$$

$$\frac{\partial i_{\mathrm{o}}^{q}}{\partial E_{\mathrm{c}}} = \frac{\sin\theta_{\mathrm{c}} \cos\varphi_{\mathrm{g}} - \cos\theta_{\mathrm{c}} \sin\varphi_{\mathrm{g}}}{Z_{\mathrm{g}}} + \frac{\sin\theta_{\mathrm{c}} \cos\varphi_{\mathrm{L}} - \cos\theta_{\mathrm{c}} \sin\varphi_{\mathrm{L}}}{Z_{\mathrm{L}}}.$$

B. Small-Signal Model in Islanding Mode

Similarly, in islanding mode, the apparent power of the converter is expressed as

$$\vec{S}_{\mathrm{DG}} = v_{\mathrm{c}} \cdot i_{\mathrm{o}}^{*} = \frac{(E_{\mathrm{c}})^{2}}{Z_{\mathrm{L}}} e^{j\varphi_{\mathrm{L}}}. \tag{A5}$$

According to (A2, A3, and A5) and [29] and [30], the small-signal model of the system in islanding mode is established as

$$(N_1 \cdot N_2 \cdot N_3 - I) \cdot \begin{bmatrix} \Delta\theta_{\mathrm{c}} \\ \Delta E_{\mathrm{c}} \end{bmatrix} = 0 \tag{A6}$$

where the matrixes N_1, N_2, and N_3 are

$$N_1 = \begin{bmatrix} -\frac{G_{\mathrm{PI}}^{P} G_{\mathrm{lpf}}(s)}{s} & -\frac{G_{\mathrm{PI}}^{Q}(s) \cdot G_{\mathrm{lpf}}(s) k_{\mathrm{f}}}{s(1-k_{\mathrm{e}})} \\ 0 & -\frac{G_{\mathrm{PI}}^{Q}(s) \cdot G_{\mathrm{lpf}}(s)}{1-k_{\mathrm{e}}} \end{bmatrix},$$

$$N_3 = \begin{bmatrix} -E_{\mathrm{c}} \sin\theta_{\mathrm{c}} & \cos\theta_{\mathrm{c}} \\ E_{\mathrm{c}} \cos\theta_{\mathrm{c}} & \sin\theta_{\mathrm{c}} \\ \frac{\partial i_{\mathrm{o}}^{d}}{\partial \theta_{\mathrm{c}}} & \frac{\partial i_{\mathrm{o}}^{d}}{\partial E_{\mathrm{c}}} \\ \frac{\partial i_{\mathrm{o}}^{q}}{\partial \theta_{\mathrm{c}}} & \frac{\partial i_{\mathrm{o}}^{q}}{\partial E_{\mathrm{c}}} \end{bmatrix}$$

$$N_2 = \begin{bmatrix} 1.5i_{\mathrm{o}}^{d} & 1.5i_{\mathrm{o}}^{q} & 1.5v_{\mathrm{c}}^{d} & 1.5v_{\mathrm{c}}^{q} \\ -1.5i_{\mathrm{o}}^{q} & 1.5i_{\mathrm{o}}^{d} & 1.5v_{\mathrm{c}}^{q} & -1.5v_{\mathrm{c}}^{d} \end{bmatrix}, I = \begin{bmatrix} 1 & 0 \\ 0 & 1 \end{bmatrix}$$

$$\frac{\partial i_{\mathrm{o}}^{d}}{\partial \theta_{\mathrm{c}}} = E_{\mathrm{c}} (\cos\theta_{\mathrm{c}} \sin\varphi_{\mathrm{L}} - \sin\theta_{\mathrm{c}} \cos\varphi_{\mathrm{L}}) / Z_{\mathrm{L}};$$

$$\frac{\partial i_{\mathrm{o}}^{d}}{\partial E_{\mathrm{c}}} = (\cos\theta_{\mathrm{c}} \cos\varphi_{\mathrm{L}} + \sin\theta_{\mathrm{c}} \sin\varphi_{\mathrm{L}}) / Z_{\mathrm{L}};$$

$$\frac{\partial i_{\mathrm{o}}^{q}}{\partial \theta_{\mathrm{c}}} = E_{\mathrm{c}} (\sin\theta_{\mathrm{c}} \sin\varphi_{\mathrm{L}} + \cos\theta_{\mathrm{c}} \cos\varphi_{\mathrm{L}}) / Z_{\mathrm{L}};$$

$$\frac{\partial i_{\mathrm{o}}^{q}}{\partial E_{\mathrm{c}}} = (\sin\theta_{\mathrm{c}} \cos\varphi_{\mathrm{L}} - \cos\theta_{\mathrm{c}} \sin\varphi_{\mathrm{L}}) / Z_{\mathrm{L}}.$$

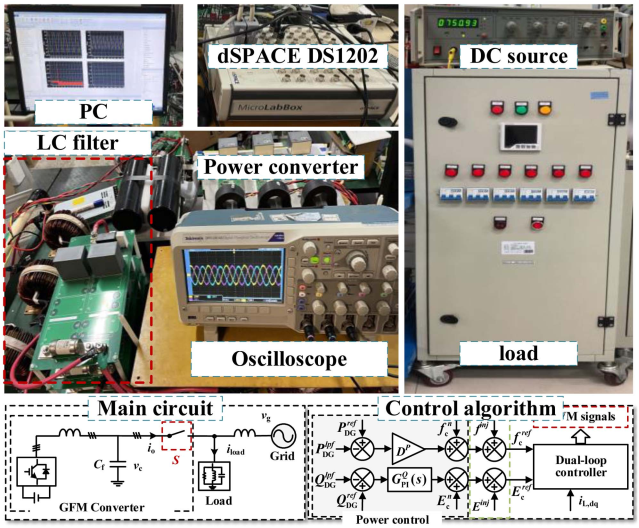

Fig. 14. Diagram of the established experimental platform.

TABLE II
SYSTEM PARAMETERS AND CONTROL PARAMETERS

Symbol	**System Parameters**	**Values**
v_{g}	Three-phase grid voltage	380 V
Z_{g}	Grid impedance	0.32 mH
v_{dc}	DC voltage	750 V
L_{f}	Filter inductor	500e-6 H
C_{f}	Filter capacitor	200e-6 F
Symbol	**Control Parameters**	**Values**
D^{P}	Droop coefficient of active power	1e-6/V
$k_{\mathrm{i,f}}^{P}$	Integral coefficient of active power	5e-7/(V.s)
D^{Q}	Proportional coefficient of reactive power	3e-4/V
$k_{\mathrm{i,f}}^{Q}$	Integral coefficient of reactive power	1e-5/(V.s)
k_{f}	Frequency perturbation coefficient	0.01 rad/(V.s)
k_{e}	Amplitude perturbation coefficient	1.005
$\Delta E_{\mathrm{c}}^{threshold}$	The boundary of output voltage amplitude fluctuation	40.0 V
$\Delta f_{\mathrm{c}}^{threshold}$	The boundaries of output voltage frequency fluctuation	0.038 Hz

C. Established RT-LAB Hardware-in-the-Loop Platform

As shown in Fig. 14, in the established experimental platform, the main circuit topology of the three-phase grid-connected converter is simulated in the real time labratory (RT-LAB). The proposed control algorithm is implemented on the actual TMS320 F28335 control board. In addition, the input/output (I/O) interface is used to realize signal interaction. The signal acquisition is realized through the AD sampling unit. Communication delay and noise interference are also taken into account in the experiment.

In addition, the adopted system parameters and control parameters are summarized in Table II.

REFERENCES

[1] T. Liu, X. Wang, F. Liu, K. Xin, and Y. Liu, “Islanding detection of grid-forming inverters: Mechanism, methods, and challenges,” *IEEE Electrif. Mag.*, vol. 10, no. 1, pp. 30–38, Mar. 2022.

[2] Ê. C. Resende, M. G. Simões, and L. C. G. Freitas, “Anti-islanding techniques for integration of inverter-based distributed energy resources to the electric power system,” *IEEE Access*, vol. 12, pp. 17195–17230, 2024.

[3] H. H. Zeineldin and J. Kirtley, “Performance of the OVP/UVP and OFP/UFP method with voltage and frequency-dependent loads,” *IEEE Trans. Power Del.*, vol. 24, no. 2, pp. 772–778, Apr. 2009.

[4] M. R. Alam, M. T. A. Begum, and K. M. Muttaqi, “Assessing the performance of ROCOF relay for anti-islanding protection of distributed generation under subcritical region of power imbalance,” *IEEE Trans. Ind. Appl.*, vol. 55, no. 5, pp. 5395–5405, Sep-Oct. 2019.

[5] M. Grebla, J. R. A. K. Yellajosula, and H. K. Høidalen, “Adaptive frequency estimation method for ROCOF islanding detection relay,” *IEEE Trans. Power Del.*, vol. 35, no. 4, pp. 1867–1875, Aug. 2020.

[6] S. De, M. V. Reddy, and R. Sodhi, “A data-driven passive islanding detection scheme,” *IEEE Trans. Ind. Appl.*, vol. 60, no. 2, pp. 3698–3709, Mar./Apr. 2024.

[7] C. R. Reddy, J. H. Choi, and B. Pangedaiah, “Absolute positive sequence voltage difference based passive islanding detection in micro grids,” *IEEE Trans. Ind. Appl.*, vol. 60, no. 3, pp. 4633–4641, May/Jun. 2024.

[8] E. Vazquez, N. Vazquez, and R. Femat, “Modified Sandia voltage shift anti-islanding scheme for distributed power generator systems,” *IET Power Electron*, vol. 13, no. 18, pp. 4226–4234, Feb. 2020.

[9] L. A. C. Lopes and H. Sun, “Performance assessment of active frequency drifting islanding detection methods,” *IEEE Trans. Energy Convers.*, vol. 21, no. 1, pp. 171–180, Mar. 2006.

[10] M. Liu, W. Zhao, Q. Wang, S. Huang, and K. Shi, “A solution to the parameter selection and current static error issues with frequency shift islanding detection methods,” *IEEE Trans. Ind. Electron.*, vol. 68, no. 2, pp. 1401–1411, Feb. 2021.

[11] D. Velasco, C. Trujillo, G. Garcera, and E. Figueres, “An active anti-islanding method based on phase-PLL perturbation,” *IEEE Trans. Power Electron.*, vol. 26, no. 4, pp. 1056–1066, Apr. 2011.

[12] M. Liu et al., “Compatibility issues with irregular current injection islanding detection methods in multi-DG units equipped with grid-connected transformers,” *IEEE Trans. Power Electron.*, vol. 37, no. 3, pp. 3599–3616, Mar. 2022.

[13] R. Bakhshi-Jafarabadi, J. Sadeh, J. d. J. Chavez, and M. Popov, “Two-level islanding detection method for grid-connected photovoltaic system-based microgrid with small non-detection zone,” *IEEE Tran. Smart Grid*, vol. 12, no. 2, pp. 1063–1072, Mar. 2021.

[14] R. Bakhshi-Jafarabadi, J. Sadeh, and M. Popov, “Maximum power point tracking injection method for islanding detection of grid-connected photovoltaic systems in microgrid,” *IEEE Trans. Power Del.*, vol. 36, no. 1, pp. 168–179, Feb. 2021.

[15] K. Kim, Y. Park, J. Lee, and S. Ju, “Control strategy of energy storage system for islanding detection based on load analysis with machine learning,” *IEEE Trans. Smart Grid*, vol. 15, no. 5, pp. 4719–4730, Sep. 2024.

[16] J. He and Y. W. Li, “Analysis, design, and implementation of virtual impedance for power electronics interfaced distributed generation,” *IEEE Trans. Ind. Appl.*, vol. 47, no. 6, pp. 2525–2538, Nov./Dec. 2011.

[17] Y. Li, Y. Gu, and T. C. Green, “Revisiting grid-forming and grid-following inverters: A duality theory,” *IEEE Trans. Power Syst.*, vol. 37, no. 6, pp. 4541–4554, Nov. 2022.

[18] Y. Liu, X. Chen, Z. Chen, X. Shi, L. Lin, and Z. Wang, “Research on the effects of grid-forming control on islanding detection effectiveness of distributed energy resources,” in *Proc. 2023 IEEE 2nd Int. Power Electron. Application Symp.*, Guangzhou, China, 2023, pp. 1592–1598.

[19] D. Lin et al., “Performance evaluation of islanding detection for distributed energy resources with grid support functions,” *IEEE Trans. Ind. Appl.*, vol. 61, no. 6, pp. 9602–9614, Nov./Dec. 2025, doi: 10.1109/TIA.2025.3576734.

[20] H. Zheng, Z. Liu, R. An, J. Liu, T. Wu, and Z. Lin, “An islanding detection method using synchronized small-AC-signal injection for grid-forming inverters in microgrids,” *IEEE Trans. Power Electron.*, vol. 38, no. 5, pp. 5816–5831, May 2023.

[21] H. J. Kim, M. S. Kim, and E. S. Lee, “Enhanced islanding detection for GFM and GFL inverters using negative sequence current injection,” *IEEE Trans. Ind. Electron.*, vol. 72, no. 10, pp. 10119–10129, Oct. 2025, doi: 10.1109/TIE.2025.3549103.

[22] A. K. Dubey, A. Kumar, J. P. Mishra, and N. R. C., “Grid forming power converter equipped with SAPF and active islanding detection capabilities employing SOSF-SOFLL based synchronization,” *IEEE Trans. Ind. Appl.*, vol. 61, no. 3, pp. 4626–4635, May–Jun. 2025.

[23] Z. Ye, A. Kolwalkar, Y. Zhang, P. Du, and R. Walling, “Evaluation of anti-islanding schemes based on nondetection zone concept,” *IEEE Trans. Power Electron.*, vol. 19, no. 5, pp. 1171–1176, Sep. 2004.

[24] U. Markovic, D. Chrysostomou, P. Aristidou, and G. Hug, “Impact of inverter-based generation on islanding detection schemes in distribution networks,” *Electric Power Syst. Res.*, vol. 190, 2021, Art. no. 106610.

[25] P. Rodríguez, A. Luna, R. S. Muñoz-Aguilar, I. Etxeberria-Otadui, R. Teodorescu, and F. Blaabjerg, “A stationary reference frame grid synchronization system for three-phase grid-connected power converters under adverse grid conditions,” *IEEE Trans. Power Electron.*, vol. 27, no. 1, pp. 99–112, Jan. 2012.

[26] X. Wang, “Optimization strategy of DSOGI-PLL precision under harmonic interference conditions,” in *Proc. 2020 IEEE Sustain. Power Energy Conf.*, Chengdu, China, 2020, pp. 852–857.

[27] *IEEE standard for interconnection and interoperability of distributed en- energy resources with associated electric power systems interfaces*, IEEE Standard 1547-2018 (Revision IEEE Standard 1547-2003), 2018.

[28] U. Markovic, D. Chrysostomou, P. Aristidou, and G. Hug, “Impact of inverter-based generation on islanding detection schemes in distribution networks,” *Elec. Pow. Sys. Res.*, vol. 190, Jan. 2021, Art. no. 106610.

[29] E. A. A. Coelho, P. C. Cortizo, and P. F. D. Garcia, “Small signal stability for single phase inverter connected to stiff ac system,” in Proc. *Conf. Rec. IEEE IAS Annu. Meeting*, 1999, pp. 2180–2187.

[30] E. A. A. Coelho, P. C. Cortizo, and P. F. D. Garcia, “Small-signal stability for parallel-connected inverters in stand-alone AC supply systems,” *IEEE Trans. Ind. Appl.*, vol. 38, no. 2, pp. 533–542, Mar./Apr. 2002.

Bingtao Zhang (Student Member, IEEE) received the B.Sc. degree in marine electrical and electronic engineering and the M.Sc. degree in electrical engineering from Shanghai Maritime University, Shanghai, China, in 2019 and 2022, respectively. He is currently working toward the Ph.D. degree in electrical engineering with Tianjin University, Tianjin, China.

His current research interests include optimal control and power quality management of microgrids and distributed power generation.

Jinwei He (Member, IEEE) received the B.Sc. degree in electrical engineering from Southeast University, Nanjing, China, in 2005, the M.Sc. degree in electrical engineering from the Institute of Electrical Engineering, Chinese Academy of Sciences, Beijing, China, in 2008, and the Ph.D. degree in electrical engineering from the University of Alberta, Edmonton, AB, Canada, in 2013.

In September 2015, he joined Tianjin University, Tianjin, China, where he is currently a Professor with the School of Electrical and Information Engineering. His research interests include power electronics for microgrid and distributed power generation.

Lucheng Hong (Senior Member, IEEE) received the B.S. degree in electrical engineering from the School of Electrical Engineering, Southeast University, Nanjing, China, in 2007, and the Ph.D. degree in electrical engineering from the Department of Electrical Engineering, Tsinghua University, Beijing, China, in 2013.

He is currently working with the School of Electrical and Information Engineering, Tianjin University, Tianjin, China. His research interests include operation, planning, and analysis of power electronics-based power system and AI applications in power systems.